

Exchange striction induced thermal Hall effect in van der Waals antiferromagnet MnPS₃

Heejun Yang,¹ Gyungchoon Go,² Jaena Park,¹ Se Kwon Kim,² and Je-Geun Park^{1,*}

¹Department of Physics and Astronomy, Seoul National University, Seoul 08826, Korea

²Department of Physics, Korea Advanced Institute of Science and Technology, Daejeon 34141, Korea

* Corresponding author: jgpark10@snu.ac.kr

Abstract

The thermal Hall effect has emerged as an ideal probe for investigating topological phenomena of charge-neutral excitation. Notably, it reveals crucial aspects of spin-lattice couplings that have been difficult to access for decades. However, the exchange striction mechanism from a lattice-induced change in exchange interaction has often been ignored in thermal Hall experiments. MnPS₃ can offer a platform to study exchange striction on the thermal Hall effect due to its significant spin-lattice coupling and field-induced non-collinear spin configuration. Our thermal transport data show distinct temperature and field dependence of longitudinal thermal conductivity (κ_{xx}) and thermal Hall effect (κ_{xy}). By using detailed theoretical calculation, we found that the inclusion of the exchange striction is essential for a better description of both κ_{xx} and κ_{xy} . Our result demonstrates the importance of the exchange striction mechanism for a complete understanding of the magnon-phonon-driven thermal Hall effect.

I . INTRODUCTION

The topological nature of spin excitations has recently become the focus of recent extensive studies, both experiments and theories, whose potential consequences go beyond the horizon of fundamental understanding and spintronics [1,2]. Due to their charge neutrality, the thermal Hall effect (THE) is considered a promising experimental technique to investigate this exotic aspect of magnons, otherwise fundamental quasiparticles of magnetism [3]. Early measurements of THE have been reported in various magnetic insulators: ferromagnetic spin configurations [4–7] and frustrated magnets [8–17]. However, recent unexpected THE observed in non-magnetic materials [18–21] demonstrate the potentially important role of phonons in THE studies. Another closely related recent report is that strong spin fluctuations can significantly modify thermal transport in the paramagnetic phase of magnetic insulators like hexagonal manganite YMnO_3 [22]. This new development requires one to put spins and phonons on equal footing, which poses a severe, experimental and theoretical, challenge to our understanding of heat transport, including THE.

Therefore, spin-lattice coupling has become an urgent and timely issue in understanding thermal transport in general and THE specifically. For example, recent experimental works, including cuprates, proposed a significant role of spin-lattice coupling for THE [23–32]. Here, one has to note that there are two fundamental mechanisms for spin-lattice coupling. One is the single-ion magnetostriction type of spin-lattice coupling that arises from the modulation of crystal fields surrounding magnetic ions [33–36]. Incidentally, it has been suggested as the source of several THE experiments [7,37,38]. Another equally important mechanism is exchange striction, which is induced by a spatial modulation of magnetic ions changing the strength of exchange interaction [39]. In particular, the exchange striction of Heisenberg interaction could be applicable to a wide range of magnetic systems, since the spin-orbit coupling is not, in principle, required for this mechanism [40]. Indeed, several inelastic neutron and X-ray studies have been done to realize the importance of the exchange striction [41–47]. Several theoretical studies of THE based on exchange striction have been suggested, accordingly [48,49]. Nevertheless, experimentally, it is still an unanswered question how the exchange striction mechanism produces THE for a given system, begging for comprehensive studies in the context of THE data analysis.

Here, two-dimensional (2D) layered magnets, known as van der Waals magnets, seem to be an ideal test ground with strong spin-lattice coupling. In particular, antiferromagnetic TMPS_3 (TM = Mn, Fe, and Ni) has been reported to have highly enhanced spin-lattice coupling [50–56]. As a member of TMPS_3 materials, MnPS_3 is an ideal material for investigating the exchange striction affecting THE for the following reasons. First, MnPS_3 consists of 2D honeycomb layers of Mn^{2+} ions [Fig. 1(a)], with a Néel-type antiferromagnetic ground state dominated by Heisenberg interaction [57,58]. As two opposite directions of magnon THE cancel out in for the Heisenberg model [59], it is natural to consider spin-lattice coupling for finite THE in MnPS_3 [36,60]. Next, Raman studies on MnPS_3 observed that the 155 cm^{-1} peak shifts drastically at the Néel temperature (T_N) [50–52], indicating significant spin-lattice coupling. Lastly, the magnetic ground state of MnPS_3 involves Mn^{2+} moments tilted away from the z-axis (out-of-plane direction) at an angle of 8° [61]. Due to this tilting, a non-collinear spin configuration can be induced by applying the magnetic field along the z-axis, as described in the right side of Fig. 1(a). Notably, this non-collinearity is necessary for magnon-phonon hybridization via the exchange striction by Heisenberg interaction [39]. All three considerations put MnPS_3 in a unique position for the THE study regarding exchange striction.

This study presents thermal transport measurement data of MnPS_3 , a 2D honeycomb Néel-type antiferromagnet. Our experimental results revealed the distinct field dependence of longitudinal thermal conductivity (κ_{xx}) and finite thermal Hall conductivity (κ_{xy}). To analyze the experimental data, we constructed a model Hamiltonian with terms included for both types of spin-lattice coupling: single-ion

magnetostriction and exchange striction. Based on these comprehensive studies, we conclude that both exchange striction and single-ion magnetostriction play distinct roles in the magnon-phonon-driven THE of MnPS₃.

II. EXPERIMENTAL METHODS

High-quality single crystals of MnPS₃ were grown by the chemical vapor transport method. Manganese powder (99.95%, Alfa Aesar), red phosphorus ($\geq 99.99\%$, Sigma-Aldrich), and sulfur powder (99.98%, Sigma-Aldrich) were mixed in the stoichiometric ratio with 5 wt% of extra sulfur within an argon atmosphere [62,63]. The mixture was sealed into a quartz ampule, and the quartz ampule was put into a horizontal two-zone furnace with a temperature difference of 780 and 700 °C for seven days. Then, the quartz ampule was cooled to room temperature over two days. Several green plate-like hexagonal-shaped crystals of MnPS₃ were obtained from the quartz ampule. The typical size of the crystals was $3 \times 3 \times 0.1$ mm³. Energy-dispersive X-ray (EDX) spectroscopy (Quantax 100, Bruker & EM-30, Coxem) confirmed the stoichiometry of the sample as Mn:P:S = 0.988:0.991:3.021. The magnetization (M) of MnPS₃ sample was measured using MPMS-XL5 (Quantum Design) by applying the magnetic field along the $z(c^*)$ -axis.

Thermal transport measurement was performed by the standard steady-state method using one heater and three thermometers. In this study, we employed custom-made SrTiO₃ parallel plate capacitors as thermometers to minimize errors from high magnetic fields and performed *in situ* calibrations [64]. The heat current was applied along the $xy(ab)$ -plane, and the magnetic field was applied along the $z(c^*)$ -axis. Three thermometers measured longitudinal (ΔT_x) and transverse (ΔT_y) temperature differences simultaneously. Under the isothermal condition, the field dependence of ΔT_x data was collected with a slowly varying field sweep. On the other hand, for ΔT_y measurement, a static magnetic field was applied in a step-by-step mode, and every data point was taken by averaging ΔT_y for a few minutes to avoid error possibly coming from the magnetocaloric effect. After that, we antisymmetrized ΔT_y data with respect to the magnetic fields to eliminate longitudinal contamination in ΔT_y due to contact misalignment. Resulting ΔT_x and antisymmetrized ΔT_y data were converted into κ_{xx} and κ_{xy} respectively, using Fourier's law of heat conduction. Further experimental details are presented in the Supplemental Material [65].

III. RESULTS

As seen in Fig. 1(b), the magnetization (M) data of our MnPS₃ sample reproduced several key features found in the previous report [71]. Firstly, the temperature dependence of M shows a broad maximum at around 120 K, implying a short-range spin-spin correlation [72]. Next, we can find a sharp cusp at 79 K [see the inset of Fig. 1(b)], which indicates T_N . Both field cooling and zero-field cooling measurements showed no discernible difference, consistent with previous study [73]. Note that our M data showed a negligibly small Curie tail in the low-temperature range, which supports the high quality of our MnPS₃ crystals.

As shown in Fig. 1(c), the temperature dependence of κ_{xx} exhibits general features of phonon thermal conductivity with a single peak around 20 K and a monotonic decrease for $T > 20$ K [74]. When applying a field of 9 T, we observed apparent suppression of κ_{xx} at low temperatures below 50 K. Although κ_{xx} seems to display a smooth change as the temperature crosses T_N , we can also observe a small cusp around T_N [see the inset of Fig. 1(c)]. This small anomaly is quite consistent with the

Raman studies reporting drastic shifts of 155 cm^{-1} peak at T_N , indicating significant spin-lattice coupling in MnPS_3 [50–52].

Fig. 1(d) also shows κ_{xy} as a function of temperature with a negative peak around 20 K. However, its size rapidly diminishes as the temperature approaches T_N , exhibiting a cusp instead of the nearly smooth behavior observed in κ_{xx} . For $T > T_N$, the temperature dependence of κ_{xy} is much weaker than in the magnetically ordered phase, representing almost flat κ_{xy} up to 200 K. These observations lead us to assume that the long-range magnetic ordering is crucial for finite κ_{xy} in MnPS_3 . The small remnant κ_{xy} signals in the supposedly paramagnetic phase above T_N are likely to be due to short-range fluctuations as proposed by recent THE studies [75,76].

As seen in Fig. 2(a), we present the magnetization (M) data as a function of the magnetic field obtained at various temperature points. For $T \ll T_N$, a spin-flop transition exhibits a sharp step-like increase in M around 4 T. As the temperature is increased further, the step-like increase of M becomes more moderate, eventually turning into a linear behavior with respect to the magnetic field. Consequently, it becomes harder to identify the spin-flop transition above 50 K from the M measurement alone. This field-linear behavior of M has been maintained up to 200 K.

Fig. 2(b) shows the detailed field dependence of magneto-thermal conductivity defined as $\Delta\kappa_{xx}(H)/\kappa_{xx}(0) \equiv [\kappa_{xx}(H) - \kappa_{xx}(0)]/\kappa_{xx}(0)$. The complex behavior can be divided into three temperature ranges. First, κ_{xx} gets increased slightly at the low field range for $T \ll T_N$ before falling sharply during the spin-flop transition. Next, for $0.5T_N < T < 1.5T_N$, κ_{xx} decreases even at the low field range. In addition, we can only see a small cusp around the spin-flop transition rather than a large suppression. Note that this cusp becomes less distinct as the temperature increases and is absent for $T > T_N$. Finally, for $T > 1.5T_N$, κ_{xx} increases again across the entire field range.

Fig. 2(c) displays field dependence of κ_{xy} data. For $T \ll T_N$, we could only obtain noisy negative κ_{xy} data exhibiting monotonic field response, due to the small signal size and the resolution limit of our experimental setup [64]. However, at slightly higher temperatures, we could observe a hump around 4.5 T in addition to the negative background. This hump quickly diminishes as the temperature increases. For $T > 0.5T_N$, it becomes challenging to identify the hump, and κ_{xy} becomes field-linear above T_N .

IV. DISCUSSIONS

A. Debye-Callaway model fitting for κ_{xx} data

The temperature dependence of κ_{xx} can be characterized by various scattering mechanisms of heat carriers [74]. For the phonon-dominant κ_{xx} case, the Debye-Callaway model is usually a standard starting point for figuring out the detailed phonon scattering mechanisms [77]. With the Debye-Callaway model, the phonon thermal conductivity can be written as follows:

$$\kappa_{xx} = \frac{k_B^4}{2\pi^2 v_D \hbar^3} T^3 \int_0^{T_D/T} \frac{x^4 \exp(x)}{[\exp(x) - 1]^2} \tau(\omega, T) dx, \quad (1)$$

where k_B (\hbar) is the Boltzmann (the reduced Planck) constant, T_D (v_D) is the Debye temperature (the group velocity of acoustic phonons) estimated from the Debye model, $\tau^{-1}(\omega, T)$ is the scattering rate of the phonon, ω is the frequency of the phonon, and $x = \hbar\omega/k_B T$. According to the Debye model, the

relationship between T_D and v_D is given as $T_D = v_D \frac{\hbar}{k_B} (6\pi^2 n)^{1/3}$, where n is the number of atoms per unit volume. For MnPS₃, T_D has been estimated at 177 K [78].

Representative scattering sources for phonon heat conduction can be listed as follows [74]: sample boundary ($\tau_{BD}^{-1} = v_D/d$), linear defects ($\tau_{LD}^{-1} = A_0\omega$), point defects ($\tau_{PD}^{-1} = A_1\omega^4$), and Umklapp process ($\tau_U^{-1} = A_2\omega^2 T \exp(-T_D/bT)$), where d represents a typical dimension of the system, b is the characteristic constant for the Umklapp process, and A_0 , A_1 and A_2 are free parameters. Then, $\tau^{-1}(\omega, T)$ can be approximated by a sum of possible scattering sources following Matthiessen's rule,

$$\tau^{-1}(\omega, T) = \tau_{BD}^{-1} + \tau_{LD}^{-1} + \tau_{PD}^{-1} + \tau_U^{-1}. \quad (2)$$

To minimize the model, we fixed d as 1 mm as the typical sample size and used conventional value for $b = 2\sqrt[3]{N} \sim 5.43$, where N is the number of atoms in a unit cell [22].

Hence, we tried to fit the experimental κ_{xx} data taken with 0 T using three free parameters A_0 , A_1 and A_2 via least-square criterion. Our best-fit result can be seen as the black solid curve in Fig. 1(c). For the fitting procedure, we excluded the data points around T_N ; we used the data points for $T < 0.5T_N$ and $T > 1.5T_N$. The main reason is that the fitting quality worsened when we fully included the data points around T_N . In the end, we obtained the following parameter set $A_0 = 4.32 \times 10^{-5}$, $A_1 = 3.99 \times 10^{-44} \text{ s}^3$, and $A_2 = 4.10 \times 10^{-18} \text{ s/K}$, which are comparable to those values from recent studies employing the Debye-Callaway model [22,29,79]. The experimental data was quite consistent with the fitting result around 20 K. However, we also note that the κ_{xx} data decreases faster than the fitting curve above 40 K.

As shown in Fig. 1(c), the suppressed behavior of κ_{xx} data as compared to the Debye-Callaway model of Eq. (2) demonstrates the existence of additional phonon scattering sources. Interestingly, a recent inelastic neutron study reported that magnetic excitations of MnPS₃ persist up to 200 K, indicating robust short-range spin-spin correlations even above T_N [80]. Therefore, phonon scattering by spin fluctuations could also be considered since the suppression of κ_{xx} was severe around the T_N , implying significant spin-lattice coupling in MnPS₃ [22]. Although we can achieve better κ_{xx} fitting by obtaining detailed information on spin-lattice coupling via *ab-initio* calculation [81,82], it would be beyond the scope of our study, calling for future works.

B. Correlation between spin-flop transitions and thermal transport coefficients

As displayed in Figs. 2(b) and (c), the field dependences of both κ_{xx} and κ_{xy} show some anomalies around 4.5 T, which seems related to the spin-flop transition. For a detailed comparison between the spin-flop transition and the anomalies in κ_{xx} and κ_{xy} , we first provide the contour plot of dM/dH , the derivative of M with respect to magnetic field [see Fig. 3(a)]. We could define the spin-flop transition by choosing the field point for the maximum value of dM/dH at each temperature. With this definition, the spin-flop transition happens around 4 T at the lowest temperature. When the temperature increases, we can observe that the spin-flop transition occurs at slightly larger magnetic fields. Above 60 K, we could not resolve the spin-flop transition via M measurement due to the limited field range of our magnetometer.

Next, Fig. 3(b) provides the contour plot of $d\kappa_{xx}/dH$, the field-derivative of κ_{xx} . The blue colored area represents anomalies of κ_{xx} , i.e., sharp suppression. We also plotted field points for the maximum value of both dM/dH and $|d\kappa_{xx}/dH|$ together on Fig. 3(b). Interestingly, temperature dependences of these field points are comparable to each other, indicating a close correlation between the spin-flop transition and anomalies of κ_{xx} . Unfortunately, the contour plot of $d\kappa_{xy}/dH$ could not be provided due to coarse data points. Nevertheless, we can repeatedly observe the hump of κ_{xy} at 4.5 T for the low-temperature region [see Fig. 2(c)]. Since the spin-flop transition happens around 4.5 T

below 50 K, we could conclude that the anomalies of κ_{xy} are also closely related to the spin-flop transition.

C. Linear spin-wave theory for κ_{xy} data

Berry curvature has been regarded as a primary source of THEs via charge-neutral excitations, since non-zero Berry curvature can induce additional transverse motion of wave packets analogous to anomalous Hall effect of electronic system [83]. Hence, we tried analyzing our data via Berry curvature scenario first. Considering all the realistic scenarios, magnons could be a main candidate for THE for the magnetically ordered phase. For Néel-type honeycomb antiferromagnet, it is known that non-zero bond-dependent exchange interactions are essential for finite κ_{xy} [84]. However, as reported in several magnetic insulators, the size of κ_{xy} due to magnons often increases as the temperature rises and collapses quickly near the magnetic phase transition [4,5,7]. This is because the nontrivial Berry curvature is usually concentrated around the Brillouin zone (BZ) boundary [85–87], where the energy scale is similar to T_N . In MnPS₃ the magnon energy at the BZ boundary is approximately 11 meV [57]. Therefore, the resulting κ_{xy} would increase up to T_N , which is inconsistent with our experimental data.

Another candidate worth considering is the magnon-phonon hybrid excitation [34–36,48,49,88]. When magnon and phonon modes cross each other, the non-zero spin-lattice coupling could open a gap at the crossing point, resulting in magnon-phonon hybridizations and the finite Berry curvature [see Fig. 4(a)]. In most cases, the coupling between the acoustic phonon branch and low-lying magnon near the BZ center would mainly affect the low-temperature range of κ_{xy} . For instance, the latest study of V₁₃ explained the enlarged size of κ_{xy} around 20 K by including the spin-lattice coupling after finding that a magnon-only model cannot explain the experimental data [7]. As our κ_{xy} also exhibits a prominent peak around 20 K, it is reasonable to expect that magnon-phonon hybridization could play a significant role for THE in MnPS₃.

To analyze the experimental results, we employed linear spin-wave theory (LSWT) and calculated magnon-phonon hybridization numerically. To simplify the analysis, we assumed a perfect honeycomb lattice of Mn²⁺ ions despite very tiny distortion on honeycomb structure of actual MnPS₃ system. We also carried out our calculations for the monolayer limit, which can be justified by the negligibly small interlayer coupling [57].

Our magnetic Hamiltonian (\mathcal{H}_m) consists of Heisenberg interactions (J_n), easy-axis anisotropy (D), and Zeeman term,

$$\mathcal{H}_m = \sum_{\langle ij \rangle_n} J_n \mathbf{S}_i \cdot \mathbf{S}_j + D \sum_i (\hat{\mathbf{n}} \cdot \mathbf{S}_i)^2 - g \mu_B \mu_0 H \sum_i S_i^z, \quad (3)$$

where \mathbf{S}_i is the spin vector of the i -th site, $\hat{\mathbf{n}} = \sin 8^\circ \hat{\mathbf{x}} + \cos 8^\circ \hat{\mathbf{z}}$ is a unit vector necessary to reproduce the ground state of MnPS₃ exhibiting 8° of canting from the z-axis. g , μ_B , μ_0 , and H denote g -factor, Bohr magneton, vacuum permeability, and external magnetic field applied along the z-axis, respectively. Throughout this study, we put x(z)-axis parallel to the crystallographic $a(c^*)$ -axis [see Fig. 1(a)]. We used $S = 5/2$, $J_1 = 1.54$ meV, $J_2 = 0.14$ meV, $J_3 = 0.36$ meV, and $D = -0.00215$ meV as taken from the previous reports [58,59], and $g = 2$ from recent electron spin resonance study [89]. The spin configurations under the finite magnetic field applied along the z-axis were obtained through classical energy minimization.

Next, the phonon Hamiltonian (\mathcal{H}_p) is

$$\mathcal{H}_p = \sum_i \frac{\mathbf{p}_i^T \mathbf{p}_i}{2m} + \frac{1}{2} \sum_{i,j} \mathbf{u}_i^T K(\mathbf{R}_i - \mathbf{R}_j) \mathbf{u}_j, \quad (4)$$

where $\mathbf{u}_i(\mathbf{p}_i)$ is the displacement (conjugate momentum) vector of i -th Mn^{2+} ion and K is a spring constant. To simplify the model, we ignored non-magnetic ions and only considered K for the 1st nearest-neighbor bonds. Hence, \mathbf{R}_i is equilibrium position of i -th Mn^{2+} ion, and $K(\mathbf{R}_i - \mathbf{R}_j)$ is a spring constant between i -th and j -th Mn^{2+} ions. Note that, by choosing suitable K , our acoustic phonon branch is comparable to the result of a recent *ab-initio* study [65,90].

For the spin-lattice coupling, we considered two mechanisms for our minimum model, as discussed in the introduction: single-ion magnetostriction ($\mathcal{H}_{\text{mp,SI}}$) and exchange striction ($\mathcal{H}_{\text{mp,ex}}$) [39].

$\mathcal{H}_{\text{mp,SI}}$ reads in the hexagonal lattice [91]:

$$\begin{aligned} \mathcal{H}_{\text{mp,SI}} = & B_1 \sum_i \left[(S_i^x)^2 \mathcal{E}_i^{xx} + (S_i^y)^2 \mathcal{E}_i^{yy} + (S_i^x S_i^y + S_i^y S_i^x) \mathcal{E}_i^{xy} \right] + B_2 \sum_i \left[(S_i^z)^2 (\mathcal{E}_i^{xx} + \mathcal{E}_i^{yy}) \right] \\ & + B_3 \sum_i \left[(S_i^y S_i^z + S_i^z S_i^y) \mathcal{E}_i^{yz} + (S_i^x S_i^z + S_i^z S_i^x) \mathcal{E}_i^{xz} \right], \end{aligned} \quad (5)$$

where $\mathcal{E}_i^{\mu\nu}$ is a one-ion strain [65,92], $B_1 = -\frac{B^Y}{2}$, $B_2 = -\frac{B^Y}{4} - B^\alpha$, and $B_3 = -\frac{B^\epsilon}{2}$ with $B^\alpha = \frac{\sqrt{3}}{2} B^{\alpha,1,2} - \frac{1}{4} B^{\alpha,2,2}$. Here, the coupling constant $B^{\alpha,1,2}$ represents the volume change, $B^{\alpha,2,2}$ is for change in the ratio between the crystallographic a - and c -axes, B^Y is for shear motion in the ab -plane, and B^ϵ is for shear motion in planes, including the c^* -axis [93]. Note that in LSWT B_3 only couples to the out-of-plane vibrational motion while B_1 and B_2 only do to in-plane motions.

We can now derive $\mathcal{H}_{\text{mp,ex}}$ by performing the Taylor-series expansion of the exchange interaction as a function of the interatom distance vector [39]. In principle, various types of exchange interactions can be expanded by Taylor-series resulting in spin-lattice coupling, such as Heisenberg, Dzyaloshinskii-Moriya, or Kitaev-like interactions. However, it is expected that $\mathcal{H}_{\text{mp,ex}}$ of Heisenberg interaction would be dominant for MnPS_3 due to high-spin configuration of Mn^{2+} ion which possesses weak spin-orbit coupling effects [81]. Therefore, we only considered the case of J_1 for simplicity as follows:

$$\mathcal{H}_{\text{mp,ex}} = J_1 \alpha_{\text{ex}} \sum_{\langle ij \rangle_1} \left[(\mathbf{u}_i - \mathbf{u}_j) \cdot \frac{\mathbf{r}_{ij}}{|\mathbf{r}_{ij}|^2} \right] (\mathbf{S}_i \cdot \mathbf{S}_j), \quad (6)$$

where \mathbf{r}_{ij} is the vector connecting two 1st nearest-neighbor Mn^{2+} ions and α_{ex} is a dimensionless coupling constant that can be obtained from the pressure dependence of 1st nearest-neighbor bond length and T_N using the following formula [41]: $\alpha_{\text{ex}} = \frac{|\mathbf{r}_{ij}(P_0)|}{T_N(P_0)} \cdot \frac{(\partial T_N / \partial P)}{(\partial |\mathbf{r}_{ij}| / \partial P)}$. As we are assuming a monolayer of Mn^{2+} ions, $\mathcal{H}_{\text{mp,ex}}$ only describes the coupling between spins and in-plane vibration. Therefore, in-plane uniaxial pressure (P_{ab}) study is required for estimating α_{ex} in our case. Unfortunately, only the hydrostatic pressure (P_h) studies have been reported for MnPS_3 [94,95] giving $\alpha_{\text{ex}} \sim -47$. Interestingly, the previous observation that $\partial T_N / \partial P_{ab}$ is several times larger than $\partial T_N / \partial P_h$ in $\text{Cr}_2\text{Ge}_2\text{Te}_6$, another 2D van der Waals magnet [96], we think, justifies our estimate of $|\alpha_{\text{ex}}|$ for MnPS_3 .

By diagonalizing the total Hamiltonian $\mathcal{H}_{\text{tot}} = \mathcal{H}_m + \mathcal{H}_p + \mathcal{H}_{\text{mp,SI}} + \mathcal{H}_{\text{mp,ex}}$, we can obtain the band dispersion and Berry curvature. We then calculated κ_{xy} using the following formula [83]:

$$\kappa_{xy} = -\frac{k_B^2 T}{\hbar(2\pi)^2 d_c} \sum_{\mathbf{k}} \sum_{\lambda=1}^{N_{\text{tot}}} c_2[\rho(E_{\lambda,\mathbf{k}})] \Omega_{\lambda,\mathbf{k}}, \quad (7)$$

where $d_c = 6.49 \text{ \AA}$ is the thickness of the honeycomb layer [97], N_{tot} is the number of total bands, $\Omega_{\lambda,\mathbf{k}}$ is the Berry curvature of the λ -th energy level at \mathbf{k} -point $E_{\lambda,\mathbf{k}}$, and $c_2[\rho(E_{\lambda,\mathbf{k}})]$ is the weight function of the Bose-Einstein distribution $\rho(E_{\lambda,\mathbf{k}}) = [\exp(E_{\lambda,\mathbf{k}}/k_B T) - 1]^{-1}$. During the calculation, the temperature is reduced by a mean-field calculation of $T_N = \frac{1}{3k_B} S(S+1)(3J_1 - 6J_2 + 3J_3)$ [57]. To identify the role of each spin-lattice coupling constant clearly, we considered only the out-of-plane vibration for B^ϵ ($N_{\text{tot}} = 4$) and in-plane vibration for other coupling constants ($N_{\text{tot}} = 6$). We present further details in the Supplemental Material [65].

First, we calculated κ_{xy} as a function of the magnetic field by including each coupling constant separately [Fig. 4(b)]. In our theoretical studies, finite κ_{xy} was only found for the B^γ and B^ϵ cases, which shows an anomaly around the spin-flop transition. Upon closer inspection, the B^γ term reproduces the hump shape as in the experimental data rather than the pulse shape given by B^ϵ . This implies that in-plane vibration is essential for THE in MnPS₃, which is consistent with the recent Raman study [52]. However, note that the monotonic negative background of the experimental THE data could not be reproduced by B^γ only case. Below, the inclusion of the exchange striction will be shown to reproduce the monotonic negative background.

Next, we checked how κ_{xy} changes when two different kinds of coupling constants are included simultaneously. For simplicity, we considered only the in-plane vibration since B^γ is essential to reproduce the hump shape of κ_{xy} at the spin-flop transition. Firstly, we found that combining B^γ and B^α only changed the size and sign of κ_{xy} at the spin-flop transition [see Fig. 4(c)]. For instance, when B^γ and B^α have the same sign, the anomaly of κ_{xy} becomes increased in the negative direction. On the contrary, when B^γ and B^α have the opposite sign each other, the anomaly of κ_{xy} becomes enhanced in the positive direction. Unfortunately, the negative background of κ_{xy} could not be reproduced yet.

Interestingly, when combining B^γ and α_{ex} , we can reproduce the monotonic background, as shown in Fig. 4(d), in addition to the hump. To be more specific, the negative background of κ_{xy} was obtained when the signs of the B^γ and α_{ex} are the same. On the other hand, when the signs of the B^γ and α_{ex} are opposite each other, the positive background prevails. Note that the strength of monotonic background is proportional to the size of α_{ex} . From this, we can conclude that $\mathcal{H}_{\text{mp,S1}}$ and $\mathcal{H}_{\text{mp,ex}}$ are crucial to reproduce the hump at the spin-flop transition and the negative background of κ_{xy} , respectively.

Lastly, by choosing the appropriate size of parameters ($B^\gamma = -0.04 \text{ meV/\AA}^2$, $B^\alpha = -0.25B^\gamma$, and $\alpha_{\text{ex}} = -3 \cdot 47$) comparable to the previous studies [35,36,39,60], we also calculated κ_{xy} at different temperature points [Fig. 4(e)]. Interestingly, the computational results qualitatively reproduce our experimental data well: with increasing temperature, the relative size of the hump around the spin-flop transition becomes smaller compared to the size of the negative background.

To further investigate the role of α_{ex} to achieve the negative background of κ_{xy} when combining B^γ and α_{ex} , we compared the band dispersion and Berry curvature for two different cases at the magnetic field of 9 T in Fig. 5. When displaying the band dispersion, we employed the parameter $p_{\lambda,\mathbf{k}}^{\text{ph}}$ which

indicates the degree of the phonon nature of the λ -th mode at the momentum \mathbf{k} , e.g., $p_{\lambda,\mathbf{k}}^{\text{ph}} = 1$ for a pure phonon, $p_{\lambda,\mathbf{k}}^{\text{ph}} = 0$ for a pure magnon, and $0 < p_{\lambda,\mathbf{k}}^{\text{ph}} < 1$ for hybridized modes [45]. In this study, we have assigned λ to each mode in descending order in $E_{\lambda,\mathbf{k}}$. On the other hand, we only provided the Berry curvature of the lowest energy band since THE is mainly characterized by the lowest band for the low-temperature range.

The first case is the B^{γ} only model. As expected, magnon-phonon hybridization occurs at magnon-phonon crossing points [see Fig. 5(a)]. The resulting Berry curvature is shown in Fig. 5(c), in which the Berry curvature is concentrated along a star-shape with six corners. The next case is for combining B^{γ} and α_{ex} with the same sign. As seen in Fig. 5(b), the magnon-phonon hybridization becomes stronger, showing a clear visible gap. The resulting Berry curvature is given in Fig. 5(d). The most obvious difference compared to the B^{γ} only case is that the Berry curvature hot-spots can be seen at each corner of the star shape. Note that four of them are positively signed, and the others are negatively signed. According to Eq. (7), κ_{xy} is negatively proportional to the Berry curvature. Hence, it is natural to consider that the negative background of κ_{xy} would come from positively signed Berry curvature hot-spots.

Despite a successful description of the overall field dependence of κ_{xy} , we acknowledge that there is still a discrepancy at a quantitative level. Note that a similar discrepancy was also found in other recent THE studies [7,38]. We think that this discrepancy could be mainly due to the oversimplified \mathcal{H}_{p} used for our theoretical studies. In particular, considering phonons due to all non-magnetic ions like P and S of MnPS₃ would be an important but demanding natural next step forward, as demonstrated for a couple of triangular systems [39,41,45].

Another way to improve the data analysis is to consider other mechanisms. Firstly, we can consider whether the THE mechanism of non-magnetic SrTiO₃ applies to MnPS₃, since a small remnant κ_{xy} signal persists in the paramagnetic phase up to 200 K. However, it is known that a huge dielectric constant ($\sim 10^4$) is essential for THE of SrTiO₃ [98], which is not the case with MnPS₃ [99]. On the other hand, magnetic dipolar interaction could be an additional channel of spin-lattice coupling, resulting in Berry curvature [88]. In addition, phonon skew-scattering by magnetic excitations or defects can be an alternative scenario, as suggested by the latest THE theories [76,100,101]. Advanced computational techniques such as nonlinear spin-wave theory or *ab-initio* calculation would be required [81,82,102], and all these go beyond the scope of the current work and will be the subject of future studies.

D. Estimating field dependence of phonon dominant κ_{xx}

In the last part, we tried to investigate the field dependence of κ_{xx} by using the Boltzmann transport equation [74] with magnon-phonon hybridized bands

$$\kappa_{xx} \propto \sum_{\mathbf{k}} \sum_{\lambda=1}^{N_{\text{tot}}} \left[E_{\lambda,\mathbf{k}} \frac{\partial \rho(E_{\lambda,\mathbf{k}})}{\partial T} \right] v_{\lambda,\mathbf{k}}^2 \tau_{\lambda,\mathbf{k}}, \quad (8)$$

where $v_{\lambda,\mathbf{k}}$ and $\tau_{\lambda,\mathbf{k}}$ are the group velocity and relaxation time, respectively. The factors $\left[E_{\lambda,\mathbf{k}} \frac{\partial \rho(E_{\lambda,\mathbf{k}})}{\partial T} \right] v_{\lambda,\mathbf{k}}^2$ and $\tau_{\lambda,\mathbf{k}}$ in Eq. (8) are mainly influenced by detailed band structure and scattering processes, respectively. In principle, below T_{N} , κ_{xx} includes the phonon (κ_{xx}^{ph}) and magnon (κ_{xx}^{mag})

contributions. Nevertheless, we would like to assume that κ_{xx}^{mag} is negligible in the case of MnPS₃, since the $\kappa_{xx}(T)$ data of Fig. 1(c) already show representative phonon behavior and magnon heat transport often requires significant exchange interactions ($J \sim 1500$ K) [103,104].

To estimate phonon contribution (κ_{xx}^{ph}) from magnon-phonon hybridized excitations, we tried a similar approach to that introduced in the recent thermal transport study [105]: we multiplied $p_{\lambda,\mathbf{k}}^{\text{ph}}$ to Eq. (8). For details see the Supplemental Material [65]. In general, $\tau_{\lambda,\mathbf{k}}$ is determined by various scattering sources such as sample boundary, point defect, and others [74]. Here we assumed $\tau_{\lambda,\mathbf{k}}$ to be constant for simplicity and calculated $\Delta\kappa_{xx}^{\text{ph}}(H)/\kappa_{xx}^{\text{ph}}(0)$ using the identical magnon-phonon coupling constants introduced in Fig. 4(e). Surprisingly, this simple calculation qualitatively captures the key features of the experimental $\Delta\kappa_{xx}(H)/\kappa_{xx}(0)$ with comparable magnitude: with increasing temperature, increasing κ_{xx} turns into decreasing κ_{xx} and the sharp suppression around the spin-flop transition fades out [left of Fig. 6]. Another remarkable point is that non-zero α_{ex} is quite essential to reproduce the decreasing κ_{xx} after the spin-flop transition around the T_N (see Fig. 6). In other words, the magnon-phonon hybridization induced by the exchange striction is crucial for longitudinal heat transport in MnPS₃ for $T < T_N$.

However, this model cannot reproduce increasing κ_{xx} data for $T > 1.5T_N$ as shown in Fig. 2(b), which is often found in the paramagnetic phase of several magnetic insulators [6,9,11,29,32,106]. Since magnon is no longer well-defined in the paramagnetic phase, it is hard to expect magnon-phonon hybridization. Hence, we can assume that the $\Delta\kappa_{xx}(H)/\kappa_{xx}(0)$ is now dominated by $\tau_{\lambda,\mathbf{k}}$ instead of $\left[E_{\lambda,\mathbf{k}} \frac{\partial \rho(E_{\lambda,\mathbf{k}})}{\partial T} \right] v_{\lambda,\mathbf{k}}^2$. A possible scenario is that the paramagnetic spin fluctuation can be a new scattering source [22,107,108], and the magnetic field suppresses the spin fluctuation, leading to an increase in κ_{xx} .

V. SUMMARY

In summary, we have carried out thermal transport measurements on MnPS₃, a Néel-type 2D honeycomb antiferromagnet. The obtained κ_{xx} shows distinct field behavior while κ_{xy} displays a monotonic field dependence with a hump around the spin-flop transition. For the numerical analysis, we considered the realistic magnetic ground state of MnPS₃ and constructed the minimum model Hamiltonian, including both types of the spin-lattice coupling on equal footing: single-ion magnetostriction ($\mathcal{H}_{\text{mp,SI}}$) and exchange striction ($\mathcal{H}_{\text{mp,ex}}$) of Heisenberg interaction. Our LSWT calculation succeeded in capturing the key features in κ_{xx} and κ_{xy} only when including $\mathcal{H}_{\text{mp,ex}}$ in addition to $\mathcal{H}_{\text{mp,SI}}$. Our result suggests that $\mathcal{H}_{\text{mp,ex}}$ should be considered on an equal footing with $\mathcal{H}_{\text{mp,SI}}$ for a complete description of the magnon-phonon-driven THE.

ACKNOWLEDGEMENTS

We thank Chaebin Kim, Seokhwan Yun, Stephen Winter, and Sang-Wook Cheong for the helpful discussions. The work at SNU is funded by the Leading Researcher Program of the National Research Foundation of Korea (Grant No. 2020R1A3B2079375). This work was also partly supported by the Ministry of Education through the core center program (2021R1A6C101B418). The work at KAIST is supported by the Brain Pool Plus Program through the National Research Foundation of Korea, funded by the Ministry of Science and ICT (2020H1D3A2A03099291) and the National Research Foundation of Korea, funded by the Korean Government via the SRC Center for Quantum Coherence in Condensed Matter (RS-2023-00207732). G.G. acknowledges support by the National Research Foundation of Korea (NRF-2022R1C1C2006578).

REFEFENCES

- [1] H. Katsura, N. Nagaosa, and P. A. Lee, Theory of the Thermal Hall Effect in Quantum Magnets, *Phys Rev Lett* **104**, 066403 (2010).
- [2] P. A. McClarty, Topological Magnons: A Review, *Annu Rev Condens Matter Phys* **13**, 171 (2022).
- [3] S. Murakami and A. Okamoto, Thermal Hall Effect of Magnons, *J Physical Soc Japan* **86**, 011010 (2017).
- [4] Y. Onose, T. Ideue, H. Katsura, Y. Shiomi, N. Nagaosa, and Y. Tokura, Observation of the Magnon Hall Effect, *Science* (1979) **329**, 297 (2010).
- [5] T. Ideue, Y. Onose, H. Katsura, Y. Shiomi, S. Ishiwata, N. Nagaosa, and Y. Tokura, Effect of lattice geometry on magnon Hall effect in ferromagnetic insulators, *Phys Rev B* **85**, 134411 (2012).
- [6] M. Hirschberger, R. Chisnell, Y. S. Lee, and N. P. Ong, Thermal Hall Effect of Spin Excitations in a Kagome Magnet, *Phys Rev Lett* **115**, 106603 (2015).
- [7] H. Zhang, C. Xu, C. Carnahan, M. Sretenovic, N. Suri, D. Xiao, and X. Ke, Anomalous Thermal Hall Effect in an Insulating van der Waals Magnet, *Phys Rev Lett* **127**, 247202 (2021).
- [8] M. Hirschberger, J. W. Krizan, R. J. Cava, and N. P. Ong, Large thermal Hall conductivity of neutral spin excitations in a frustrated quantum magnet, *Science* (1979) **348**, 106 (2015).
- [9] D. Watanabe, K. Sugii, M. Shimozawa, Y. Suzuki, T. Yajima, H. Ishikawa, Z. Hiroi, T. Shibauchi, Y. Matsuda, and M. Yamashita, Emergence of nontrivial magnetic excitations in a spin-liquid state of kagomé volborthite, *Proceedings of the National Academy of Sciences* **113**, 8653 (2016).
- [10] H. Doki, M. Akazawa, H.-Y. Lee, J. H. Han, K. Sugii, M. Shimozawa, N. Kawashima, M. Oda, H. Yoshida, and M. Yamashita, Spin Thermal Hall Conductivity of a Kagome Antiferromagnet, *Phys Rev Lett* **121**, 097203 (2018).
- [11] M. Akazawa, M. Shimozawa, S. Kittaka, T. Sakakibara, R. Okuma, Z. Hiroi, H.-Y. Lee, N. Kawashima, J. H. Han, and M. Yamashita, Thermal Hall Effects of Spins and Phonons in Kagome Antiferromagnet Cd-Kapellasite, *Phys Rev X* **10**, 041059 (2020).
- [12] Y. Kasahara et al., Majorana quantization and half-integer thermal quantum Hall effect in a Kitaev spin liquid, *Nature* **559**, 227 (2018).
- [13] J. A. N. Bruin, R. R. Claus, Y. Matsumoto, N. Kurita, H. Tanaka, and H. Takagi, Robustness of the thermal Hall effect close to half-quantization in α -RuCl₃, *Nat Phys* **18**, 401 (2022).
- [14] P. Czajka, T. Gao, M. Hirschberger, P. Lampen-Kelley, A. Banerjee, N. Quirk, D. G. Mandrus, S. E. Nagler, and N. P. Ong, Planar thermal Hall effect of topological bosons in the Kitaev magnet α -RuCl₃, *Nat Mater* **22**, 36 (2023).
- [15] H. Yang et al., Significant thermal Hall effect in the 3d cobalt Kitaev system Na₂Co₂TeO₆, *Phys Rev B* **106**, L081116 (2022).
- [16] H. Takeda, J. Mai, M. Akazawa, K. Tamura, J. Yan, K. Moovendaran, K. Raju, R. Sankar, K.-Y. Choi, and M. Yamashita, Planar thermal Hall effects in the Kitaev spin liquid candidate Na₂Co₂TeO₆, *Phys Rev Res* **4**, L042035 (2022).
- [17] M. Gillig, X. Hong, C. Wellm, V. Kataev, W. Yao, Y. Li, B. Büchner, and C. Hess, Phononic-magnetic dichotomy of the thermal Hall effect in the Kitaev material Na₂Co₂TeO₆, *Phys Rev Res* **5**, 043110 (2023).

- [18] X. Li, B. Fauqué, Z. Zhu, and K. Behnia, Phonon Thermal Hall Effect in Strontium Titanate, *Phys Rev Lett* **124**, 105901 (2020).
- [19] S. Sim, H. Yang, H.-L. Kim, M. J. Coak, M. Itoh, Y. Noda, and J.-G. Park, Sizable Suppression of Thermal Hall Effect upon Isotopic Substitution in SrTiO₃, *Phys Rev Lett* **126**, 015901 (2021).
- [20] S. Jiang, X. Li, B. Fauqué, and K. Behnia, Phonon drag thermal Hall effect in metallic strontium titanate, *Proceedings of the National Academy of Sciences* **119**, (2022).
- [21] X. Li, Y. Machida, A. Subedi, Z. Zhu, L. Li, and K. Behnia, The phonon thermal Hall angle in black phosphorus, *Nat Commun* **14**, 1027 (2023).
- [22] P. A. Sharma, J. S. Ahn, N. Hur, S. Park, S. B. Kim, S. Lee, J.-G. Park, S. Guha, and S.-W. Cheong, Thermal Conductivity of Geometrically Frustrated, Ferroelectric YMnO₃: Extraordinary Spin-Phonon Interactions, *Phys Rev Lett* **93**, 177202 (2004).
- [23] T. Ideue, T. Kurumaji, S. Ishiwata, and Y. Tokura, Giant thermal Hall effect in multiferroics, *Nat Mater* **16**, 797 (2017).
- [24] Y. Hirokane, Y. Nii, Y. Tomioka, and Y. Onose, Phononic thermal Hall effect in diluted terbium oxides, *Phys Rev B* **99**, 134419 (2019).
- [25] G. Grissonnanche et al., Giant thermal Hall conductivity in the pseudogap phase of cuprate superconductors, *Nature* **571**, 376 (2019).
- [26] G. Grissonnanche et al., Chiral phonons in the pseudogap phase of cuprates, *Nat Phys* **16**, 1108 (2020).
- [27] M.-E. Boulanger et al., Thermal Hall conductivity in the cuprate Mott insulators Nd₂CuO₄ and Sr₂CuO₂Cl₂, *Nat Commun* **11**, 5325 (2020).
- [28] L. Chen, M.-E. Boulanger, Z.-C. Wang, F. Tafti, and L. Taillefer, Large phonon thermal Hall conductivity in the antiferromagnetic insulator Cu₃TeO₆, *Proceedings of the National Academy of Sciences* **119**, (2022).
- [29] H. Yang, X. Xu, J. H. Lee, Y. S. Oh, S.-W. Cheong, and J.-G. Park, Diagonal and off-diagonal thermal conduction with resonant phonon scattering in Ni₃TeO₆, *Phys Rev B* **106**, 144417 (2022).
- [30] É. Lefrançois et al., Evidence of a Phonon Hall Effect in the Kitaev Spin Liquid Candidate α -RuCl₃, *Phys Rev X* **12**, 021025 (2022).
- [31] T. Uehara, T. Ohtsuki, M. Udagawa, S. Nakatsuji, and Y. Machida, Phonon thermal Hall effect in a metallic spin ice, *Nat Commun* **13**, 4604 (2022).
- [32] Y. Choi, H. Yang, J. Park, and J.-G. Park, Sizable suppression of magnon Hall effect by magnon damping in Cr₂Ge₂Te₆, *Phys Rev B* **107**, 184434 (2023).
- [33] C. Kittel, *Physical Theory of Ferromagnetic Domains*, *Rev Mod Phys* **21**, 541 (1949).
- [34] E. Thingstad, A. Kamra, A. Brataas, and A. Sudbø, Chiral Phonon Transport Induced by Topological Magnons, *Phys Rev Lett* **122**, 107201 (2019).
- [35] G. Go, S. K. Kim, and K.-J. Lee, Topological Magnon-Phonon Hybrid Excitations in Two-Dimensional Ferromagnets with Tunable Chern Numbers, *Phys Rev Lett* **123**, 237207 (2019).
- [36] S. Zhang, G. Go, K.-J. Lee, and S. K. Kim, SU(3) Topology of Magnon-Phonon Hybridization in 2D Antiferromagnets, *Phys Rev Lett* **124**, 147204 (2020).
- [37] N. Li et al., Magnon-polaron driven thermal Hall effect in a Heisenberg-Kitaev antiferromagnet,

- Phys Rev B **108**, L140402 (2023).
- [38] C. Xu, C. Carnahan, H. Zhang, M. Sretenovic, P. Zhang, D. Xiao, and X. Ke, Thermal Hall effect in a van der Waals triangular magnet FeCl₂, Phys Rev B **107**, L060404 (2023).
 - [39] T. Kim, K. Park, J. C. Leiner, and J.-G. Park, Hybridization and Decay of Magnetic Excitations in Two-Dimensional Triangular Lattice Antiferromagnets, J Physical Soc Japan **88**, 081003 (2019).
 - [40] Y. Tokura, S. Seki, and N. Nagaosa, Multiferroics of spin origin, Reports on Progress in Physics **77**, 076501 (2014).
 - [41] J. Oh et al., Spontaneous decays of magneto-elastic excitations in non-collinear antiferromagnet (Y,Lu)MnO₃, Nat Commun **7**, 13146 (2016).
 - [42] S. Tóth, B. Wehinger, K. Rolfs, T. Birol, U. Stuhr, H. Takatsu, K. Kimura, T. Kimura, H. M. Rønnow, and C. Rüegg, Electromagnon dispersion probed by inelastic X-ray scattering in LiCrO₂, Nat Commun **7**, 13547 (2016).
 - [43] K. Park, J. Oh, J. C. Leiner, J. Jeong, K. C. Rule, M. D. Le, and J.-G. Park, Magnon-phonon coupling and two-magnon continuum in the two-dimensional triangular antiferromagnet CuCrO₂, Phys Rev B **94**, 104421 (2016).
 - [44] T. Kim, J. C. Leiner, K. Park, J. Oh, H. Sim, K. Iida, K. Kamazawa, and J.-G. Park, Renormalization of spin excitations in hexagonal HoMnO₃ by magnon-phonon coupling, Phys Rev B **97**, 201113 (2018).
 - [45] K. Park et al., Magnetoelastic excitations in multiferroic hexagonal YMnO₃ studied by inelastic x-ray scattering, Phys Rev B **102**, 085110 (2020).
 - [46] L. Chen, C. Mao, J.-H. Chung, M. B. Stone, A. I. Kolesnikov, X. Wang, N. Murai, B. Gao, O. Delaire, and P. Dai, Anisotropic magnon damping by zero-temperature quantum fluctuations in ferromagnetic CrGeTe₃, Nat Commun **13**, 4037 (2022).
 - [47] S. Bao et al., Direct observation of topological magnon polarons in a multiferroic material, Nat Commun **14**, 6093 (2023).
 - [48] X. Zhang, Y. Zhang, S. Okamoto, and D. Xiao, Thermal Hall Effect Induced by Magnon-Phonon Interactions, Phys Rev Lett **123**, 167202 (2019).
 - [49] S. Park and B.-J. Yang, Topological magnetoelastic excitations in noncollinear antiferromagnets, Phys Rev B **99**, 174435 (2019).
 - [50] Y.-J. Sun, Q.-H. Tan, X.-L. Liu, Y.-F. Gao, and J. Zhang, Probing the Magnetic Ordering of Antiferromagnetic MnPS₃ by Raman Spectroscopy, J Phys Chem Lett **10**, 3087 (2019).
 - [51] K. Kim et al., Antiferromagnetic ordering in van der Waals 2D magnetic material MnPS₃ probed by Raman spectroscopy, 2d Mater **6**, (2019).
 - [52] D. Vaclavkova, A. Delhomme, C. Faugeras, M. Potemski, A. Bogucki, J. Suffczyński, P. Kossacki, A. R. Wildes, B. Grémaud, and A. Saúl, Magnetoelastic interaction in the two-dimensional magnetic material MnPS₃ studied by first principles calculations and Raman experiments, 2d Mater **7**, 035030 (2020).
 - [53] J.-U. Lee, S. Lee, J. H. Ryoo, S. Kang, T. Y. Kim, P. Kim, C.-H. Park, J.-G. Park, and H. Cheong, Ising-Type Magnetic Ordering in Atomically Thin FePS₃, Nano Lett **16**, 7433 (2016).
 - [54] A. McCreary, J. R. Simpson, T. T. Mai, R. D. McMichael, J. E. Douglas, N. Butch, C. Dennis, R. Valdés Aguilar, and A. R. Hight Walker, Quasi-two-dimensional magnon identification in

- antiferromagnetic FePS₃ via magneto-Raman spectroscopy, *Phys Rev B* **101**, 064416 (2020).
- [55] S. Liu et al., Direct Observation of Magnon-Phonon Strong Coupling in Two-Dimensional Antiferromagnet at High Magnetic Fields, *Phys Rev Lett* **127**, 097401 (2021).
- [56] K. Kim, S. Y. Lim, J.-U. Lee, S. Lee, T. Y. Kim, K. Park, G. S. Jeon, C.-H. Park, J.-G. Park, and H. Cheong, Suppression of magnetic ordering in XXZ-type antiferromagnetic monolayer NiPS₃, *Nat Commun* **10**, 345 (2019).
- [57] A. R. Wildes, B. Roessli, B. Lebech, and K. W. Godfrey, Spin waves and the critical behaviour of the magnetization in MnPS₃, *Journal of Physics: Condensed Matter* **10**, 6417 (1998).
- [58] A. R. Wildes, S. Okamoto, and D. Xiao, Search for nonreciprocal magnons in MnPS₃, *Phys Rev B* **103**, 024424 (2021).
- [59] R. Cheng, S. Okamoto, and D. Xiao, Spin Nernst Effect of Magnons in Collinear Antiferromagnets, *Phys Rev Lett* **117**, 217202 (2016).
- [60] G. Go, H. Yang, J.-G. Park, and S. K. Kim, Topological magnon polarons in honeycomb antiferromagnets with spin-flop transition, *Phys Rev B* **109**, 184435 (2024).
- [61] E. Ressouche, M. Loire, V. Simonet, R. Ballou, A. Stunault, and A. Wildes, Magnetoelectric MnPS₃ as a candidate for ferrotoroidicity, *Phys Rev B* **82**, 100408 (2010).
- [62] S. Lee, K.-Y. Choi, S. Lee, B. H. Park, and J.-G. Park, Tunneling transport of mono- and few-layers magnetic van der Waals MnPS₃, *APL Mater* **4**, (2016).
- [63] J.-Y. Shan, M. Ye, H. Chu, S. Lee, J.-G. Park, L. Balents, and D. Hsieh, Giant modulation of optical nonlinearity by Floquet engineering, *Nature* **600**, 235 (2021).
- [64] H.-L. Kim, M. J. Coak, J. C. Baglo, K. Murphy, R. W. Hill, M. Sutherland, M. C. Hatnean, G. Balakrishnan, and J.-G. Park, Modular thermal Hall effect measurement setup for fast-turnaround screening of materials over wide temperature range using capacitive thermometry, *Review of Scientific Instruments* **90**, (2019).
- [65] See Supplemental Material for details on experiments, numerical calculations, and additional experimental data. The Supplemental material also contains Refs. [66-70].
- [66] C. Tinsman, G. Li, C. Su, T. Asaba, B. Lawson, F. Yu, and L. Li, Probing the thermal Hall effect using miniature capacitive strontium titanate thermometry, *Appl Phys Lett* **108**, (2016).
- [67] D. H. Jones, Q. A. Pankhurst, and C. E. Johnson, Spin-wave theory of anisotropic antiferromagnets in applied magnetic fields, *Journal of Physics C: Solid State Physics* **20**, 5149 (1987).
- [68] J. H. P. Colpa, Diagonalization of the quadratic boson hamiltonian, *Physica A: Statistical Mechanics and Its Applications* **93**, 327 (1978).
- [69] T. Holstein and H. Primakoff, Field Dependence of the Intrinsic Domain Magnetization of a Ferromagnet, *Physical Review* **58**, 1098 (1940).
- [70] T. Fukui, Y. Hatsugai, and H. Suzuki, Chern Numbers in Discretized Brillouin Zone: Efficient Method of Computing (Spin) Hall Conductances, *J Physical Soc Japan* **74**, 1674 (2005).
- [71] K. Okuda, K. Kurosawa, S. Saito, M. Honda, Z. Yu, and M. Date, Magnetic Properties of Layered Compound MnPS₃, *J Physical Soc Japan* **55**, 4456 (1986).
- [72] A. R. Wildes, S. J. Kennedy, and T. J. Hicks, True two-dimensional magnetic ordering in MnPS₃, *Journal of Physics: Condensed Matter* **6**, L335 (1994).

- [73] D. H. Luong, T. L. Phan, G. Ghimire, D. L. Duong, and Y. H. Lee, Revealing antiferromagnetic transition of van der Waals MnPS₃ via vertical tunneling electrical resistance measurement, *APL Mater* **7**, (2019).
- [74] R. Berman, *Thermal Conductions in Solids* (Clarendon Press, Oxford, 1976).
- [75] H.-L. Kim, T. Saito, H. Yang, H. Ishizuka, M. J. Coak, J. H. Lee, H. Sim, Y. S. Oh, N. Nagaosa, and J.-G. Park, Thermal Hall effects due to topological spin fluctuations in YMnO₃, *Nat Commun* **15**, 243 (2024).
- [76] T. Oh and N. Nagaosa, Phonon thermal Hall effect in Mott insulators via skew-scattering by the scalar spin chirality, *arXiv:2408.01671* (2024).
- [77] J. Callaway, Model for Lattice Thermal Conductivity at Low Temperatures, *Physical Review* **113**, 1046 (1959).
- [78] Y. Takano, N. Arai, A. Arai, Y. Takahashi, K. Takase, and K. Sekizawa, Magnetic properties and specific heat of MPS₃ (M=Mn, Fe, Zn), *J Magn Magn Mater* **272–276**, E593 (2004).
- [79] S. Bao et al., Evidence for magnon-phonon coupling in the topological magnet Cu₃TeO₆, *Phys Rev B* **101**, 214419 (2020).
- [80] S. Calder, A. V. Haglund, A. I. Kolesnikov, and D. Mandrus, Magnetic exchange interactions in the van der Waals layered antiferromagnet MnPSe₃, *Phys Rev B* **103**, 024414 (2021).
- [81] R. Dhakal, S. Griffith, K. Choi, and S. M. Winter, Spin-Phonon Coupling in Transition Metal Insulators: General Computational Approach and Application to MnPSe₃, *arXiv:2407.00659* (2024).
- [82] R. Dhakal, D. A. S. Kaib, S. Biswas, R. Valenti, and S. M. Winter, Spin-Phonon Coupling in Transition Metal Insulators II: Spin-Orbital Moments, Chiral Phonons and Application to α -RuCl₃, *arXiv:2407.00660* (2024).
- [83] R. Matsumoto and S. Murakami, Theoretical Prediction of a Rotating Magnon Wave Packet in Ferromagnets, *Phys Rev Lett* **106**, 197202 (2011).
- [84] R. R. Neumann, A. Mook, J. Henk, and I. Mertig, Thermal Hall Effect of Magnons in Collinear Antiferromagnetic Insulators: Signatures of Magnetic and Topological Phase Transitions, *Phys Rev Lett* **128**, 117201 (2022).
- [85] A. Mook, J. Henk, and I. Mertig, Magnon Hall effect and topology in kagome lattices: A theoretical investigation, *Phys Rev B* **89**, 134409 (2014).
- [86] K.-S. Kim, K. H. Lee, S. B. Chung, and J.-G. Park, Magnon topology and thermal Hall effect in trimerized triangular lattice antiferromagnet, *Phys Rev B* **100**, 064412 (2019).
- [87] L. E. Chern, E. Z. Zhang, and Y. B. Kim, Sign Structure of Thermal Hall Conductivity and Topological Magnons for In-Plane Field Polarized Kitaev Magnets, *Phys Rev Lett* **126**, 147201 (2021).
- [88] R. Takahashi and N. Nagaosa, Berry Curvature in Magnon-Phonon Hybrid Systems, *Phys Rev Lett* **117**, 217205 (2016).
- [89] J. J. Abraham, Y. Senyk, Y. Shemerliuk, S. Selter, S. Aswartham, B. Büchner, V. Kataev, and A. Alfonsov, Magnetic anisotropy and low-energy spin dynamics in the van der Waals compounds Mn₂P₂S₆ and MnNiP₂S₆, *Phys Rev B* **107**, 165141 (2023).
- [90] J. Yang, Y. Zhou, Q. Guo, Y. Dedkov, and E. Voloshina, Electronic, magnetic and optical

- properties of MnPX_3 ($X = \text{S, Se}$) monolayers with and without chalcogen defects: a first-principles study, *RSC Adv* **10**, 851 (2020).
- [91] E. Callen and H. B. Callen, Magnetostriction, Forced Magnetostriction, and Anomalous Thermal Expansion in Ferromagnets, *Physical Review* **139**, A455 (1965).
- [92] W. E. Evenson and S. H. Liu, Theory of Magnetic Ordering in the Heavy Rare Earths, *Physical Review* **178**, 783 (1969).
- [93] A. E. Clark, B. F. DeSavage, and R. Bozorth, Anomalous Thermal Expansion and Magnetostriction of Single-Crystal Dysprosium, *Physical Review* **138**, A216 (1965).
- [94] W. Toyoshima, T. Masubuchi, T. Watanabe, K. Takase, K. Matsubayashi, Y. Uwatoko, and Y. Takano, Pressure dependence of the magnetic properties of MnPS_3 , *J Phys Conf Ser* **150**, 042215 (2009).
- [95] D. M. Jarvis, Structural and Magnetic Phases in Pressure-Tuned Quantum Materials, University of Cambridge (Thesis), 2020.
- [96] S. Spachmann, A. Elghandour, S. Selter, B. Büchner, S. Aswartham, and R. Klingeler, Strong effects of uniaxial pressure and short-range correlations in $\text{Cr}_2\text{Ge}_2\text{Te}_6$, *Phys Rev Res* **4**, (2022).
- [97] G. Ouvrard, R. Brec, and J. Rouxel, Structural determination of some MPS_3 layered phases ($M = \text{Mn, Fe, Co, Ni}$ and Cd), *Mater Res Bull* **20**, 1181 (1985).
- [98] J.-Y. Chen, S. A. Kivelson, and X.-Q. Sun, Enhanced Thermal Hall Effect in Nearly Ferroelectric Insulators, *Phys Rev Lett* **124**, 167601 (2020).
- [99] M. Rybak, P. E. Faria Junior, T. Woźniak, P. Scharoch, J. Fabian, and M. Birowska, Magneto-optical anisotropies of two-dimensional antiferromagnetic MnPX_3 from first principles, *Phys Rev B* **109**, 054426 (2024).
- [100] B. Flebus and A. H. MacDonald, Charged defects and phonon Hall effects in ionic crystals, *Phys Rev B* **105**, L220301 (2022).
- [101] L. Mangeolle, L. Balents, and L. Savary, Phonon Thermal Hall Conductivity from Scattering with Collective Fluctuations, *Phys Rev X* **12**, 041031 (2022).
- [102] D. Chatzichrysaifis and A. Mook, Thermal Hall Effect of Magnons from Many-Body Skew Scattering, *arXiv:2407.00423* (2024).
- [103] C. Hess, B. Büchner, U. Ammerahl, L. Colonescu, F. Heidrich-Meisner, W. Brenig, and A. Revcolevschi, Magnon Heat Transport in Doped La_2CuO_4 , *Phys Rev Lett* **90**, 197002 (2003).
- [104] C. Hess, Heat conduction in low-dimensional quantum magnets, *Eur Phys J Spec Top* **151**, 73 (2007).
- [105] C. A. Pocs, I. A. Leahy, J. Xing, E. S. Choi, A. S. Sefat, M. Hermele, and M. Lee, Generic magnetic field dependence of thermal conductivity in magnetic insulators via hybridization of acoustic phonons and spin-flip excitations, *arXiv:2401.01407* (2024).
- [106] C. A. Pocs, I. A. Leahy, H. Zheng, G. Cao, E.-S. Choi, S.-H. Do, K.-Y. Choi, B. Normand, and M. Lee, Giant thermal magnetoconductivity in CrCl_3 and a general model for spin-phonon scattering, *Phys Rev Res* **2**, 013059 (2020).
- [107] L. D. Casto et al., Strong spin-lattice coupling in CrSiTe_3 , *APL Mater* **3**, (2015).
- [108] Y. Liu et al., Polaronic Conductivity in $\text{Cr}_2\text{Ge}_2\text{Te}_6$ Single Crystals, *Adv Funct Mater* **32**, (2022).

FIGURES

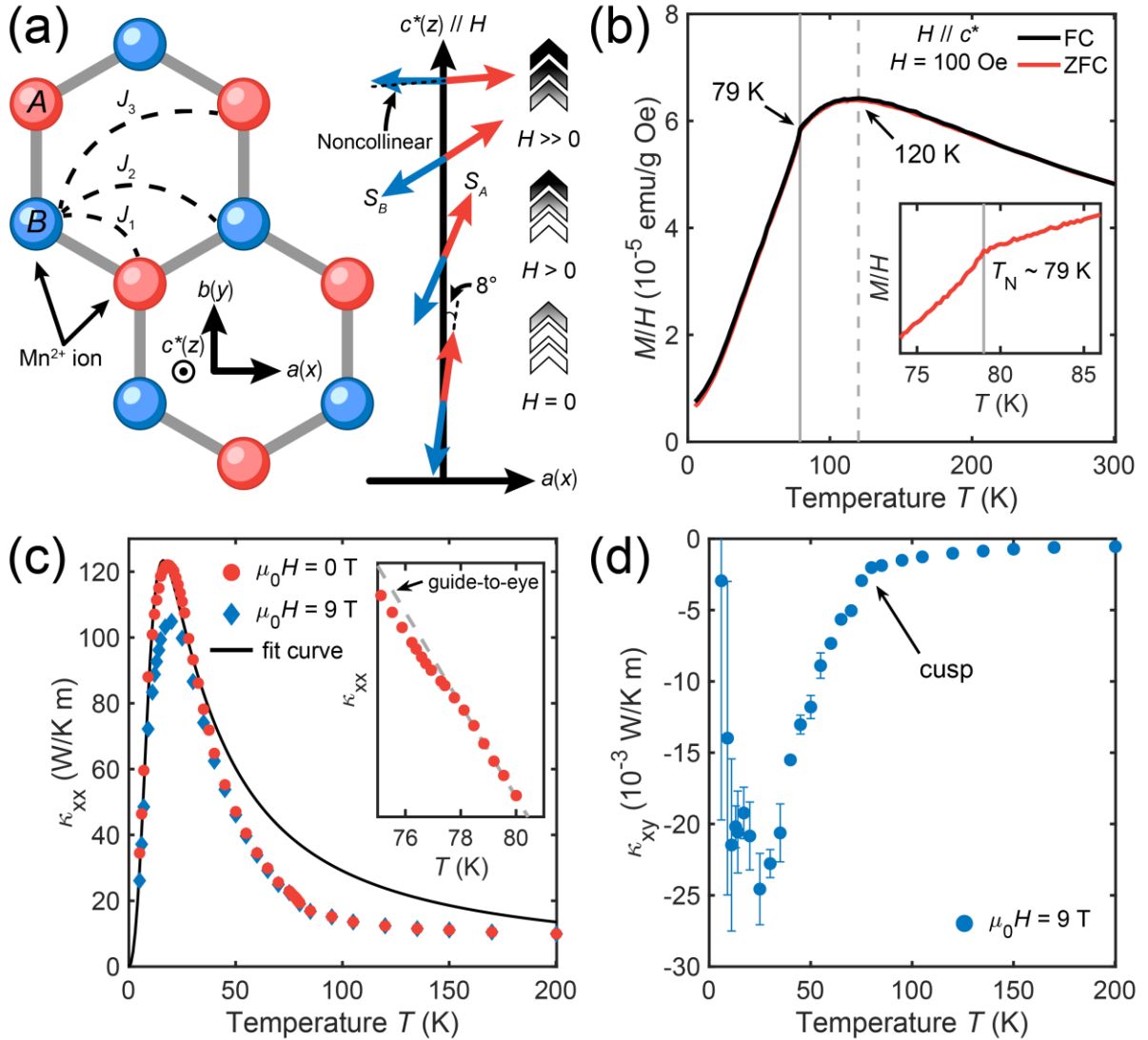


FIG. 1. (a) Left: Schematic of the Mn²⁺ honeycomb layer in MnPS₃. A and B denote two sublattices of honeycomb lattice. J_n is the exchange parameter of the n -th nearest-neighbor bond. Right: Schematic of the spin configuration under the different magnetic fields (H). The red (blue) arrow represents the magnetic moment of Mn²⁺ of the A(B)-sublattice. (b) Magnetization (M) as a function of temperature. The 100 Oe of H -field was applied along the c^* -axis. FC and ZFC represent Field-Cooled and Zero-Field-Cooled, respectively. Gray solid- and dashed- lines indicate 79 K and 120 K, respectively. The inset shows an enlarged image around T_N . (c) κ_{xx} as a function of temperature. Red circles and blue diamonds represent experimental data obtained from $\mu_0 H = 0$ T and 9 T, respectively. Black solid curve denotes the fitting result obtained from the Debye-Callaway model. Inset shows an enlarged image of κ_{xx} around T_N . Gray dashed-line is a guide-to-eye specifying small anomalies around T_N . (d) κ_{xy} as a function of temperature at $\mu_0 H = 9$ T. Error bars are standard deviations obtained from multiple measurements.

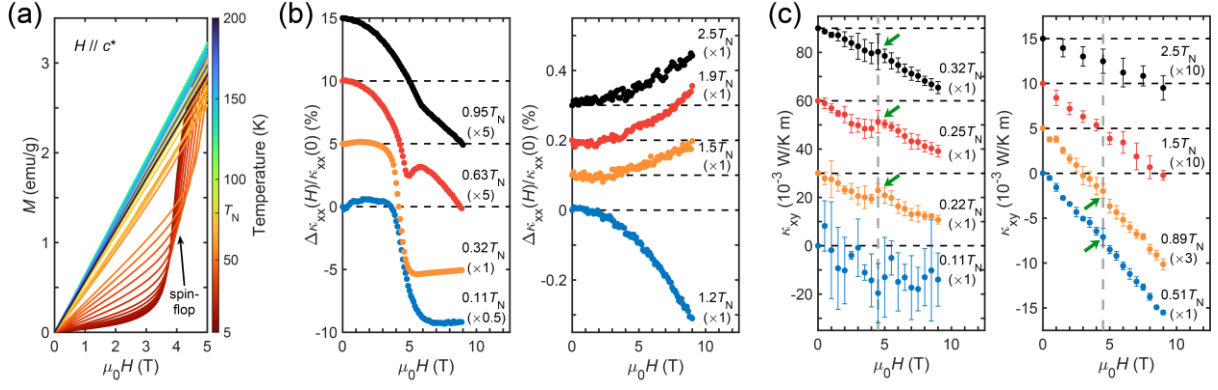


FIG. 2. (a) The magnetic field (H) dependence of magnetization (M) at several temperature points. (b) The magneto-thermal conductivity $\Delta\kappa_{xx}(H)/\kappa_{xx}(0)$ defined as $[\kappa_{xx}(H) - \kappa_{xx}(0)]/\kappa_{xx}(0)$ as a function of H -field. (c) The H -field dependence of κ_{xy} . The gray dashed-line is guide-to-eye specifying $\mu_0 H = 4.5$ T. Green arrows indicate anomalies observed around the spin-flop transition. Error bars are standard deviations obtained from multiple measurements. For clarity of (b) and (c), the data are shifted upwards and multiplied by a scaling factor in parenthesis.

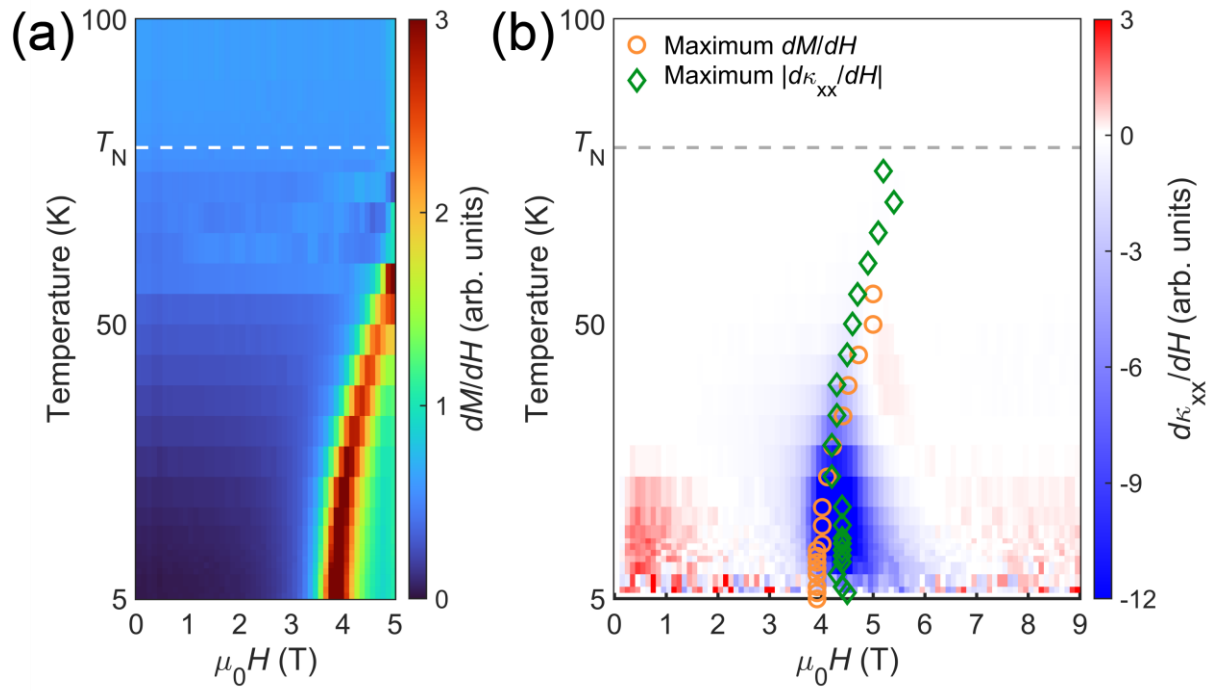


FIG. 3. The contour plots of (a) dM/dH , derivative of magnetization (M) with respect to H -field, and (b) $d\kappa_{xx}/dH$, κ_{xx} differentiated with respect to H -field. The x - and y -axes denote H -field and temperature, respectively. Orange circles and green diamonds in (b) represent H -field values possessing maximum of dM/dH and $|d\kappa_{xx}/dH|$, respectively.

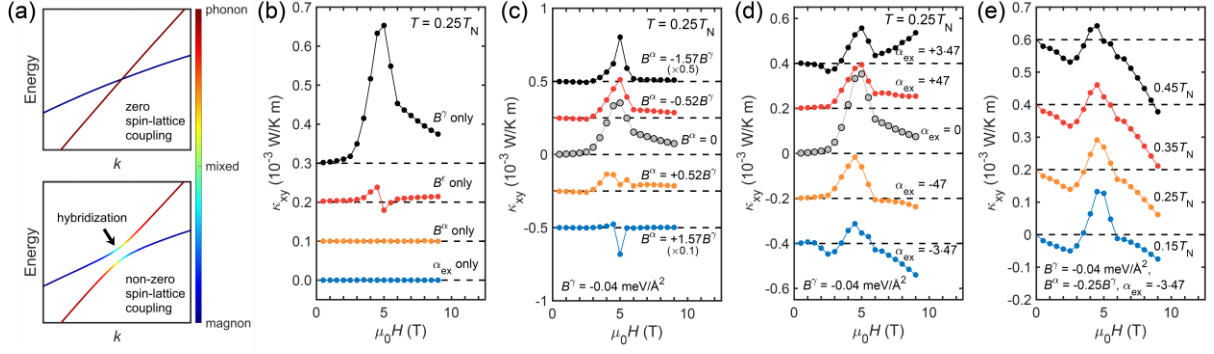


FIG. 4. (a) Schematic of magnon-phonon hybridization with respect to spin-lattice coupling. Red (blue) color denotes phonon (magnon)-like mode and green color represents hybridized mode. Upper panel: Magnon and phonon crossing point show no gap without spin-lattice coupling. Lower panel: Magnon and phonon crossing point are gapped by non-zero spin-lattice coupling. (b)-(e) Numerical calculation result of κ_{xy} with the following spin-lattice coupling constants. (b) Each result obtained from $B^\gamma = -0.04 \text{ meV/\AA}^2$, $B^\epsilon = -0.028 \text{ meV/\AA}^2$, $B^\alpha = -0.01 \text{ meV/\AA}^2$, and $\alpha_{\text{ex}} = -47$, respectively. (c) $B^\gamma = -0.04 \text{ meV/\AA}^2$, $B^\alpha = -1.57B^\gamma, -0.52B^\gamma, +0.52B^\gamma, +1.57B^\gamma$, and $B^\epsilon = \alpha_{\text{ex}} = 0$. (d) $B^\gamma = -0.04 \text{ meV/\AA}^2$, $\alpha_{\text{ex}} = -3 \cdot 47, -47, +47, +3 \cdot 47$, and $B^\alpha = B^\epsilon = 0$. (e) $B^\gamma = -0.04 \text{ meV/\AA}^2$, $B^\alpha = -0.25B^\gamma$, $\alpha_{\text{ex}} = -3 \cdot 47$, and $B^\epsilon = 0$. For clarity, all the results in (b)-(e) are shifted upwards and multiplied by a scaling factor in parenthesis (multiplied unity if there is no parenthesis).

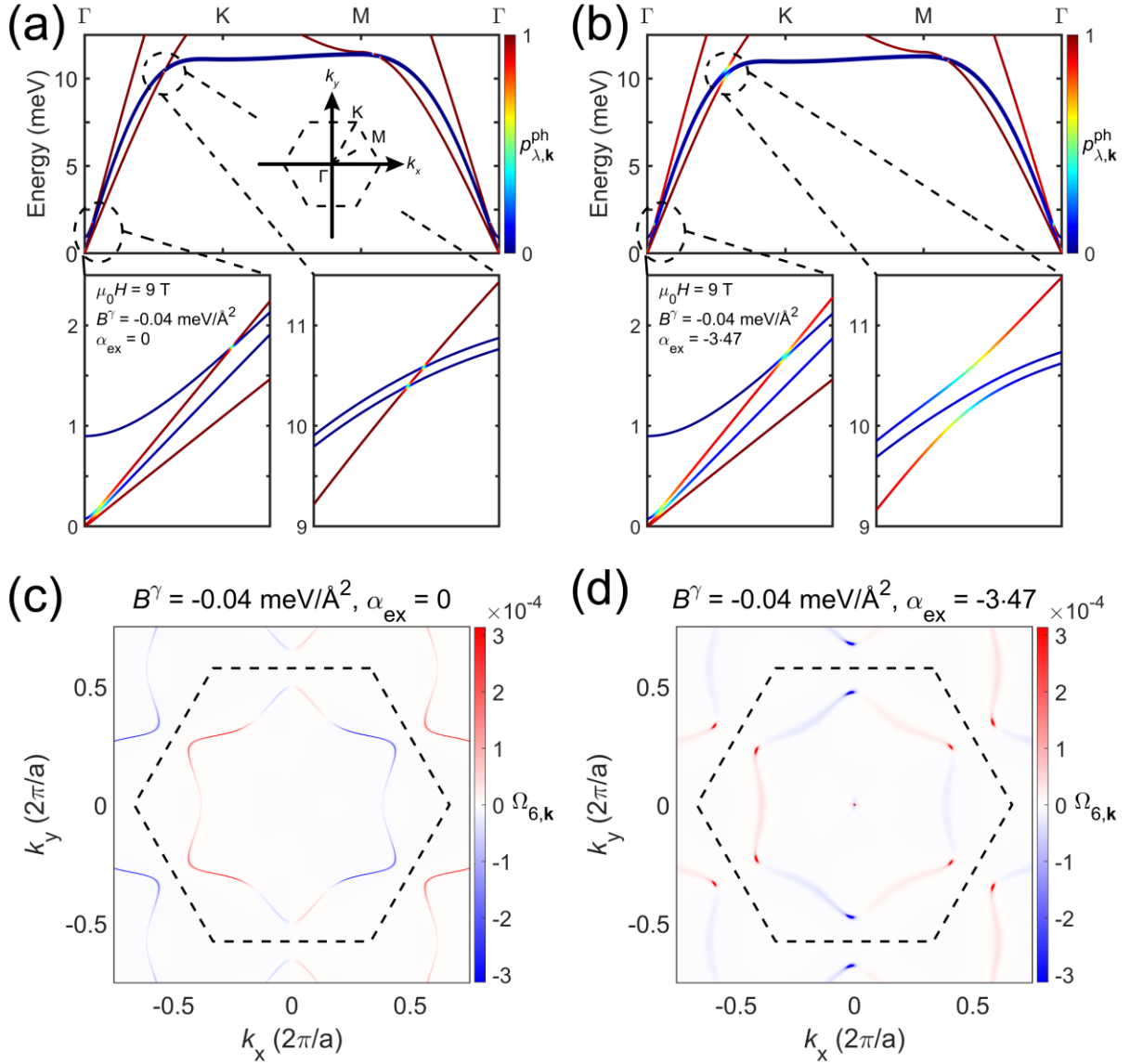


FIG. 5. The magnon and phonon band dispersions at $\mu_0 H = 9$ T obtained from (a) $B^\gamma = -0.04$ meV/Å², $\alpha_{\text{ex}} = 0$ and (b) $B^\gamma = -0.04$ meV/Å², $\alpha_{\text{ex}} = -3 \cdot 47$. Insets show enlarged image near the Γ - and K-points. The resulting Berry curvature flux of the lowest band obtained from (c) $B^\gamma = -0.04$ meV/Å², $\alpha_{\text{ex}} = 0$ and (d) $B^\gamma = -0.04$ meV/Å², $\alpha_{\text{ex}} = -3 \cdot 47$. Black dashed hexagon denotes the first Brillouin-zone boundary.

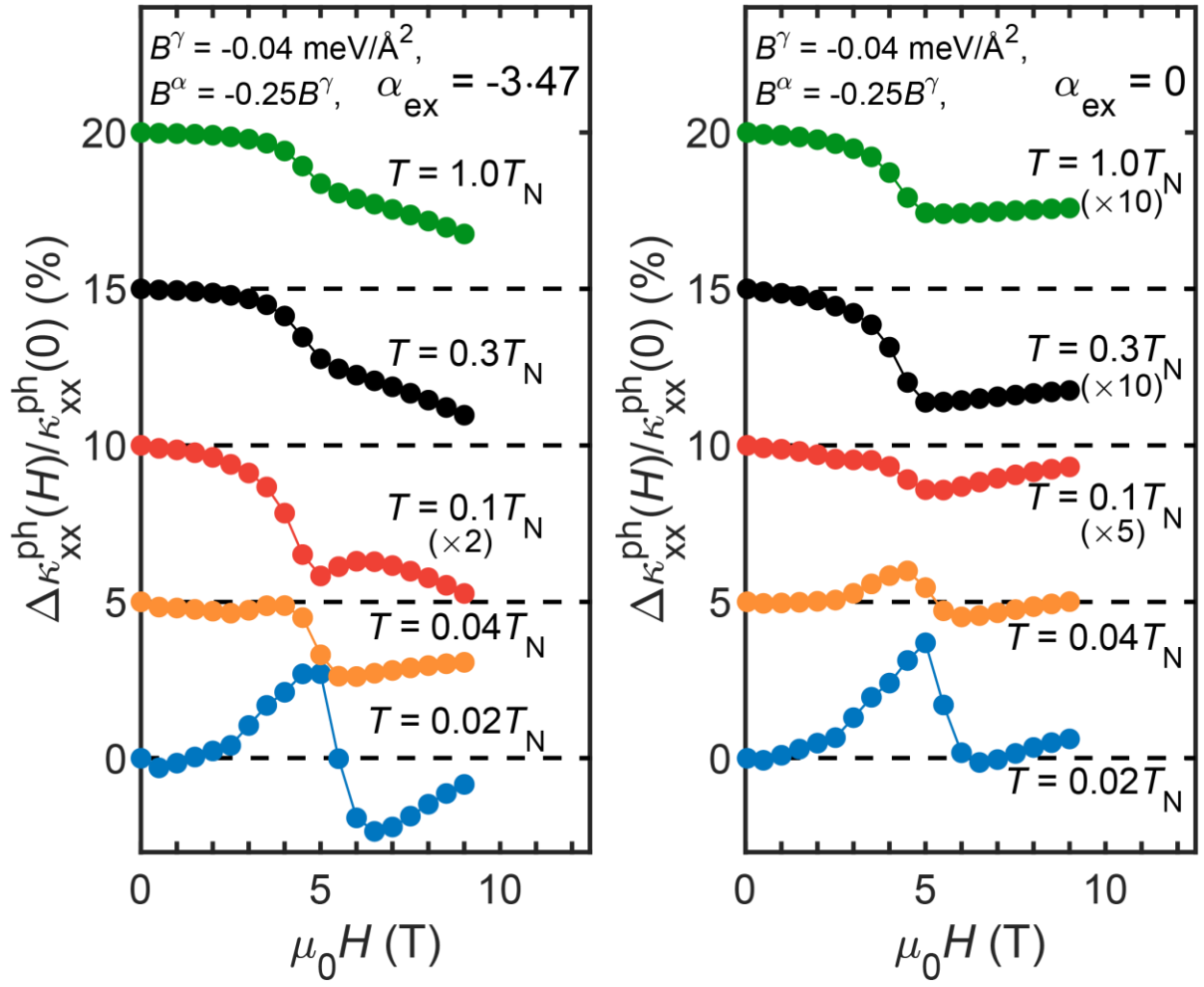


FIG. 6. Numerical calculation result of $\Delta\kappa_{xx}^{\text{ph}}(H)/\kappa_{xx}^{\text{ph}}(0)$ using the following parameter sets. Left: $B^\gamma = -0.04 \text{ meV/\AA}^2$, $B^\alpha = -0.25B^\gamma$, $\alpha_{\text{ex}} = -3.47$. Right: $B^\gamma = -0.04 \text{ meV/\AA}^2$, $B^\alpha = -0.25B^\gamma$, $\alpha_{\text{ex}} = 0$. For clarity, the results are shifted upwards and multiplied by a scaling factor in parenthesis (multiplied unity if there is no parenthesis).